
Measuring and Comparing the Hardness Factor of the MC40 Cyclotron using BPW34F Photodiodes

Cameron Simpson-Allsop

Student I.D: 1436038

Y4 Master's Report



UNIVERSITY OF
BIRMINGHAM

Project Partner:

Lydia Ram

Supervisors:

Dr. Tony Price

Dr. Kostas Nikolopoulos

March 23, 2018

Estimated Word Count: 8740

Abstract

The I-V and C-V characteristics of BPW34F photodiodes have been discussed. By utilising the NIEL scaling hypothesis, and the relation between the hardness factor and the change in leakage current, before and after 25 MeV proton irradiations, the hardness factor of the MC40 cyclotron at the University of Birmingham was found to be $\kappa_{MC40} = 2.24 \pm 0.09$, which agreed with preliminary measurements. By applying a similar study to photodiodes irradiated at the Karlsruhe Institute of Technology, a value of $\kappa_{KIT} = 2.20 \pm 0.27$ for 24 MeV protons was determined. The two values were in agreement with each other, and the currently used value of 2.2, to one standard deviation.

School of Physics and Astronomy
University of Birmingham
Birmingham, B15 2TT

Acknowledgements

I would like to thank my project partner, Lydia Ram, for all of her hard work, dedication, and organisational skills throughout the project. I would also like to thank my supervisors, Dr. T. Price and Dr. K. Nikolopoulos for their time, effort, and guidance. Furthermore, my gratitude goes to Dr. J. Thomas, Prof. P. Allport, Dr. L. Gonnella, and S. Pyatt for their greatly appreciated advice. A general thank you to the particle physics research group for granting us permission to make use of the clean rooms, and for their guidance throughout the year. Thank you to the Karlsruhe Institute of Technology for allowing us to analyse their photodiodes. A final thank you to Prof. D. Parker and the cyclotron operations team for granting us permission to perform the photodiode irradiations.

Contents

1	Introduction	4
2	Theory	4
2.1	The Silicon P-I-N Junction	5
2.2	Leakage Current Temperature Dependence	7
2.3	Capacitance - Voltage relation and Maximum Depletion	7
2.4	Radiation Damage Effects	7
2.5	The Arrhenius Relation	9
2.6	The NIEL Scaling Hypothesis	9
3	I-V Measurements	11
3.1	Pre-Irradiation Procedure	11
3.2	Pre-Irradiation Results	14
4	C-V Measurements	16
4.1	C-V Procedure	16
4.2	Determination of the Maximum Depletion Voltage	17
4.3	Maximum Depletion Voltage Variation with Proton Fluence	18
4.4	Frequency Dependence of Capacitance	19
5	Proton Irradiations	20
5.1	Irradiation Procedure	20
5.2	Beam Calibration	22
5.3	Nickel Foil Activation	23
5.4	Annealing Procedure	24
6	Determination of the Hardness Factor	26
6.1	MC40 Cyclotron Analysis	26
6.2	KIT Analysis	29
7	Conclusion and Discussion	31
Appendices		34
A	Justification of Errors	34
B	Maximum Depletion Voltage Relation to AC Frequency	35

C C–V Error Optimisation	35
D Cobalt-60 Calibration	36
E Oven Calibration and Recovery Tests	37
F Individual Data Sets for Hardness Factor Determination	37

1 Introduction

The scheduled upgrade of the LHC to the High Luminosity LHC (HL-LHC) in 2024 [1] presents new challenges in radiation damage studies. Around the world, campaigns to measure radiation hardness are being undertaken. Standard 1 MeV neutron equivalent fluences are used for the purpose of inter-facility collaboration. And, in order to convert to these fluences from experimentally determined proton fluences at given energies, a quantity known as the hardness factor is used. At the University of Birmingham, the MC40 cyclotron adopts a hardness factor value of 2.2 [2]. However, for similar energy beams, facilities have recorded differing values. For example, the Karlsruhe Institute of Technology (KIT) has recorded a value of 2.05 ± 0.61 for 24 MeV protons, with a previous assumption of 1.85 for 26 MeV protons [3]. Previous studies at the University of Birmingham have recorded a value of 1.64 ± 0.27 for 23 MeV protons [4][5]. Other studies have claimed similar values, such as 2.22 for 27 MeV protons [6, p. 107]. Tabulated values from RD50 reveal a value of ~ 2.56 for 25 MeV protons [7]. Due to these discrepancies, a conclusive result for the value of the hardness factor is needed. Furthermore, the large errors involved with such measurements mean that converting from proton fluences to 1 MeV neutron equivalent fluences introduces potential discrepancies with quoted fluences.

The aim of this project was to analyse the current-voltage ($I-V$) and capacitance-voltage ($C-V$) characteristics of BPW34F photodiodes, in both the irradiated and non-irradiated cases. This includes verifying the activation energy of silicon, and computing the maximum depletion voltage for both irradiated and non-irradiated photodiodes. The effects of annealing was also studied, and a procedure developed to anneal for a specific time and temperature with accuracy. Putting these studies together, the hardness factor of the MC40 cyclotron was determined for 25 MeV protons. By irradiating large numbers of photodiodes, the associated error was reduced, which enabled the hardness factor to be determined with relative precision. Using methods learned in this determination, a similar study was undertaken by using photodiodes irradiated at KIT, and the two values were compared.

2 Theory

Silicon photodiodes are designed to output a current based on the intensity of incoming light. Using a positive-intrinsic-negative (P-I-N) junction, the photodiode only allows current to flow readily under forward bias. Output current in the reverse biased case is referred to as leakage current.

2.1 The Silicon P–I–N Junction

A silicon P–I–N junction consists of p-type and n-type silicon in contact, with an intrinsic region in the centre. The only difference between a P–N and a P–I–N junction is the presence of the intrinsic region in-between the two materials. As the titles suggest, the p-type material has a majority of free holes, and the n-type material has a majority of free electrons. Therefore, at the boundary between the p-type and n-type materials, there is diffusion of majority carriers from both sides. A fraction of these will recombine, leaving a deficit of majority carriers in a region known as the depletion region. In the case of a P–I–N junction, this region is defined by the intrinsic region. Figure 1 shows a schematic diagram of this. For P–I–N photodiodes, the depletion region is analogous to a parallel plate capacitor, and when a sufficient reverse bias is applied, the mathematics behind it is treated as the same.

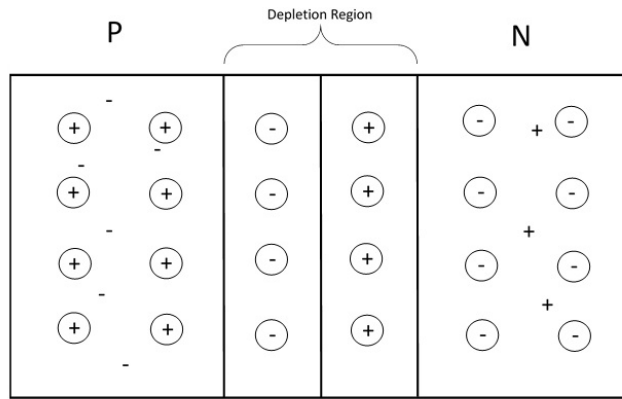


Figure 1: Diagram of a P–I–N junction with a formed depletion region.

Applying a potential difference across the depletion layer alters the relative positions of the Fermi levels, which are defined as the highest energy level for a collection of electrons at absolute zero [8]. Figure 2 shows the effect of biasing the system on the relative positions of these levels. In the event of no bias being applied, the Fermi levels are unperturbed, and energetically equal, as shown by figure 2a, allowing majority carriers to diffuse across the boundary. In the forward biased case, as shown by figure 2b, the n-type material Fermi level is moved energetically higher, meaning that electrons can readily flow across the boundary. However, this only occurs at a voltage higher than 0.6 V due to the presence of traps at the boundary [9, p. 150]. Referring to figure 1, applying an electrostatic potential across the junction has the effect of forcing the majority carriers in each material towards or away from the boundary. In the forward biased case, the electrostatic potential is applied such that that majority carriers are forced towards the boundary, and the n-type material Fermi level is moved energetically higher than the p-type material Fermi level.

Hence, the current flows readily.

In the reverse biased case, the electrostatic potential acts in the opposite direction. This means that the majority carriers in each material are forced away from the boundary, and the p-type material Fermi level is moved energetically higher than the n-type material Fermi level. Therefore, electrons cannot easily recombine with holes across the boundary, and hence, current cannot readily flow. The result of this is that the depletion region will grow until it reaches the maximum depletion voltage.

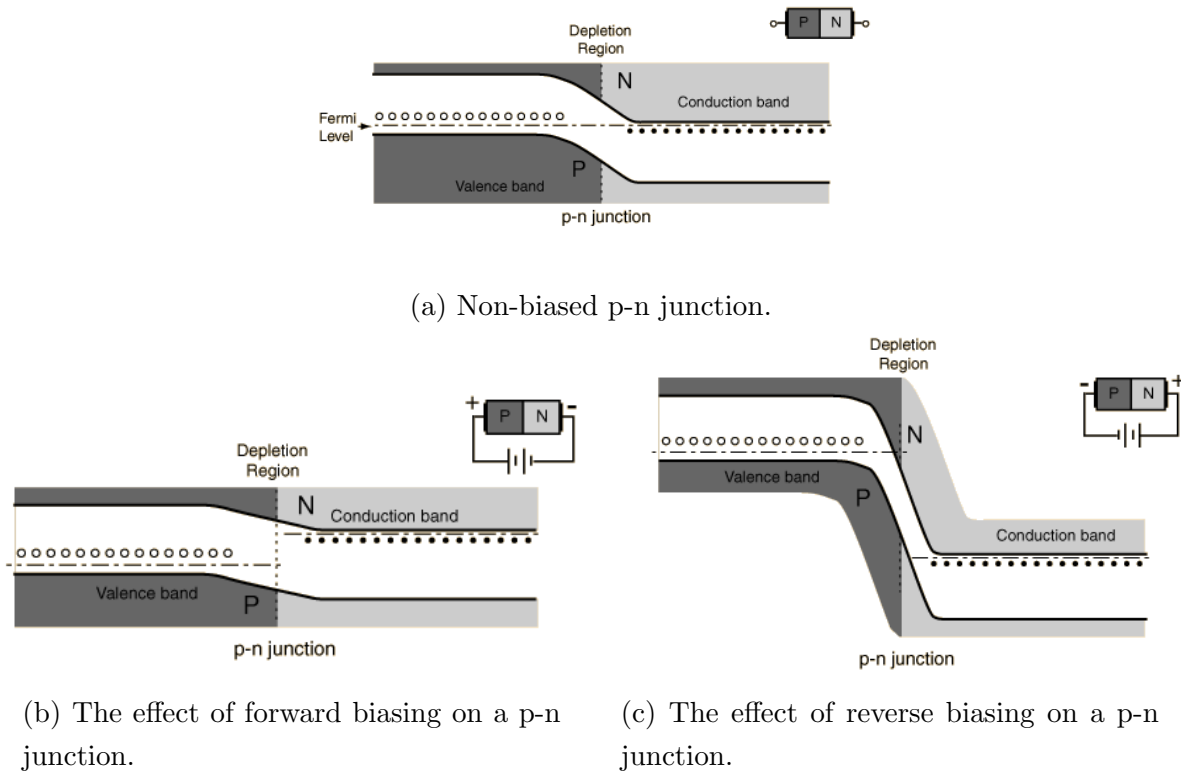


Figure 2: The difference between forward biasing and reverse biasing, in terms of the relative positions of Fermi levels with respect to the band gap, when applied to a p-n junction [10].

Under reverse bias, the system collapses when the breakdown voltage is reached. At this point, the valence band of the p-type material matches the energy level of the conduction band of the n-type material. This means, that once again, majority carriers can recombine at the boundary, and the leakage current will flow readily.

2.2 Leakage Current Temperature Dependence

The leakage current of a photodiode, $I(T)$, is dependent upon the temperature of the measurement, T , as shown by equation 1 [11, p. 26].

$$I(T_R) = I(T) \left(\frac{T_R}{T} \right)^2 e^{-\frac{E_a}{2k_B} \left[\frac{1}{T_R} - \frac{1}{T} \right]} \quad (1)$$

Where T_R is some reference temperature, $I(T_R)$ is the equivalent current at that reference temperature, E_a is the activation energy of silicon, which is closely related to the band gap energy of silicon, and all other symbols have their usual meanings.

2.3 Capacitance - Voltage relation and Maximum Depletion

As stated in section 2.1, the depletion region of the photodiode is analogous to a parallel plate capacitor. The capacitance, C , of a photodiode under a reverse bias, V , is shown by equation 2 [12, p. 38].

$$C = \frac{f \sqrt{\epsilon_{Si} \epsilon_0}}{\sqrt{V}} \quad (2)$$

Where f is a constant depending on the active area of the silicon and the number of free charge carriers, and all other symbols have their usual meanings. As an increasing reverse bias is applied, the size of the depletion region will grow, which is analogous to increasing the distance between the plates of a parallel plate capacitor. This causes the capacitance of the system to decrease. However, equation 2 is only valid up until the maximum depletion voltage is reached. At maximum depletion voltage, the depletion region will have reached its maximum size, and therefore will stop growing. This means that the capacitance will become independent of voltage, with a final value depending on the size of the depletion region. This is shown by equation 3 [11, p. 24], which is just the standard relation for parallel plate capacitors.

$$C = \frac{l^2 \epsilon_0 \epsilon_{Si}}{w} \quad (3)$$

Where l^2 is the active area of the silicon, and w is the depletion width.

2.4 Radiation Damage Effects

Protons incident on a lattice can induce radiation damage related lattice defects. Figure 3 shows a diagram of various defect types. The simplest type of lattice defect is known as a Schottky defect [13, p. 37]. Schottky defects arise when an atom is missing from its corresponding lattice site,

leaving a vacancy. Atoms surrounding the vacancy will tend to readjust their positions in order to compensate for the missing atom, which can distort the lattice. This provides a way for atoms to diffuse across the lattice with very little energy requirement. Protons that do not have enough energy to completely knock out a lattice atom and create a Schottky defect will instead induce a vacancy-interstitial, or Frenkel defect. In this case, the effected atom is dislodged, as opposed to being completely removed.

The most damaging form of lattice defect is the cluster defect. A cluster defect arises when an incident proton has enough energy to not only cause a Schottky defect, but provide enough energy to the bombarded atom, or primary knock-out atom (PKA), such that it travels through the lattice, inducing further Schottky and Frenkel defects in its wake. This process will continue until the kinetic energy of the PKA is less than that required to induce a lattice defect.

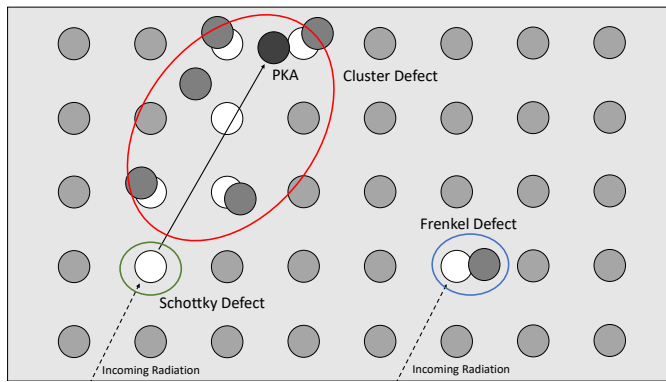


Figure 3: Diagram of radiation induced lattice defects.

Schottky defects provide a way for diffusion of atoms through a lattice with a very low energy requirement: atoms can move into the lattice vacancy with little consequence, which causes the defect to move. Lattice defects introduce the presence of new energy levels into the system, close to the middle of the band gap. Figure 4 shows a schematic diagram of processes induced by the new energy levels. Since lattice defects can be a result of radiation damage, it follows that the frequency, or number, of these processes will increase with the fluence incident on the lattice.

The most dominant process is generation, which involves the creation of an electron and a hole. Recombination is simply the process whereby the electron and hole recombine. As a result, carriers are provided for conduction. And, each process will therefore contribute charge to the overall leakage current. Hence, a radiation damaged photodiode will output a higher leakage current, when compared to the non-radiation damaged case, dependent on the degree of radiation damage in which it has incurred.

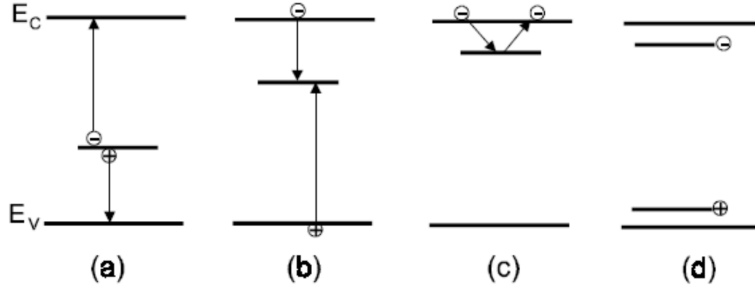


Figure 4: Schematic diagram of radiation damage induced processes: (a) generation, (b) recombination, (c) trapping, (d) compensation [12, p. 35].

2.5 The Arrhenius Relation

Annealing is the process whereby lattice defects can repair themselves over time. For example, as stated in section 2.4, atoms can diffuse and readjust their positions to counter a damaged lattice site. This can then reduce the measured leakage current of the photodiode as the degree of radiation damage decreases. The rate of annealing depends exponentially on temperature, as shown by equation 4.

$$\frac{1}{\tau} \propto e^{-\frac{E_{anneal}}{k_B T}} \quad (4)$$

Where τ is the annealing time, E_{anneal} is the activation energy for dissociation or migration [11, p. 49], T is the annealing temperature, and all other symbols have their usual meanings.

2.6 The NIEL Scaling Hypothesis

Figure 5 shows how the displacement damage function varies with energy for differing particle types. In terms of this project, the particle of interest is protons. The hardness factor is related to the displacement damage function as shown by equation 5 [11, p. 35].

$$\kappa = \frac{\int D(E)\phi(E)dE}{D(E_n = 1 \text{ MeV}) \int \phi(E)dE} \quad (5)$$

Where $\phi(E)$ is the fluence at a given energy, and $D(E_n = 1 \text{ MeV})$ is a normalizing factor. For figure 5, this factor is set to 95 MeVmb.

The change in leakage current, ΔI , before and after irradiation, for a photodiode can be expressed as shown by equation 6 [11, p. 99].

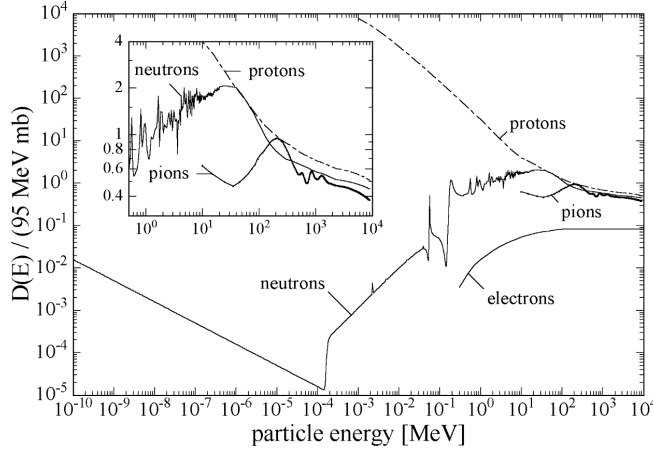


Figure 5: Displacement damage as a function of energy for varying particle types [11, p. 34].

$$\Delta I = \alpha l^2 w \phi \quad (6)$$

Where α is the current related damage rate for protons, w is the maximum depletion width, and ϕ is the incident proton fluence. Similarly, the relation for neutron equivalent fluences can be expressed as shown by equation 7.

$$\Delta I = \alpha_{neq} l^2 w \phi_{neq} \quad (7)$$

Where α_{neq} is the neutron equivalent current related damage rate, and ϕ_{neq} is the neutron equivalent fluence.

The NIEL scaling hypothesis assumes that the induced radiation damage is proportional to the displacement damage function. Therefore, the hardness factor, κ of the incident beam can be defined as shown by equation 8 [11, p. 35].

$$\kappa = \frac{\phi_{neq}}{\phi} \quad (8)$$

Since the MC40 cyclotron utilises a proton beam, ϕ_{neq} is unobtainable. Hence, by taking the ratio of equations 6 and 7, the hardness factor can be written as a ratio between the relevant current related damage rates, as shown by equation 9.

$$\kappa = \frac{\alpha}{\alpha_{neq}} \quad (9)$$

3 I-V Measurements

3.1 Pre-Irradiation Procedure

Figure 6 shows the experimental setup used to take I-V measurements. The photodiode itself was placed within an aluminium box in order to block out any electromagnetic radiation, which could interfere with the leakage current reading. A Keithley 2410 source meter was used to apply a reverse bias across the diode, which then measured and displayed the corresponding current. A thermocouple was used to record the temperature within the box, being placed close to the actual photodiode to get an accurate reading of its temperature. In order to circulate the air, and keep the temperature consistent within the box, a 5 V electric fan was used, set to a voltage of 2.6 V. This voltage was chosen because it was just high enough to provide effective air circulation, but not so high that it generated heat and affected the measurements. Initial I-V curves were taken manually. This was done to become familiar with the equipment.

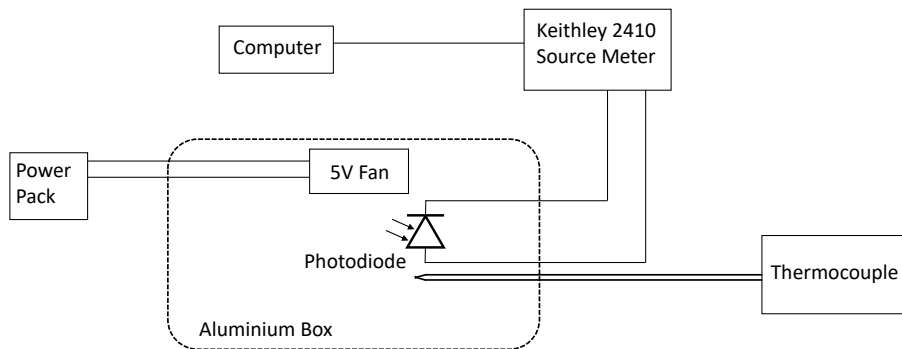


Figure 6: Schematic diagram of I-V setup.

Figure 7 shows a picture of inside the aluminium box. The photodiode, fan, and thermocouple are present. The tape serves to block out any light that could infiltrate through the gaps. The lid of the box could be closed to provide full shielding.

I-V measurements were taken by applying a reverse bias across a photodiode starting from 0 V, and reducing to -210 V in 5 V increments. After preliminary tests, the Keithley 2410 source meter was connected to a laptop. A labVIEW program was then used to take automatic I-V sweeps (courtesy of S. Flynn). For each reverse bias value, five measurements of leakage current were taken. Between each measurement, a settling time of 0.2s was applied. The benefit of using an I-V sweep program was that each curve was taken over the same time period, meaning that any effects on leakage current due to phenomena such as internal heating within the photodiode, were kept relatively constant. Furthermore, the shorter resultant time required to take a single

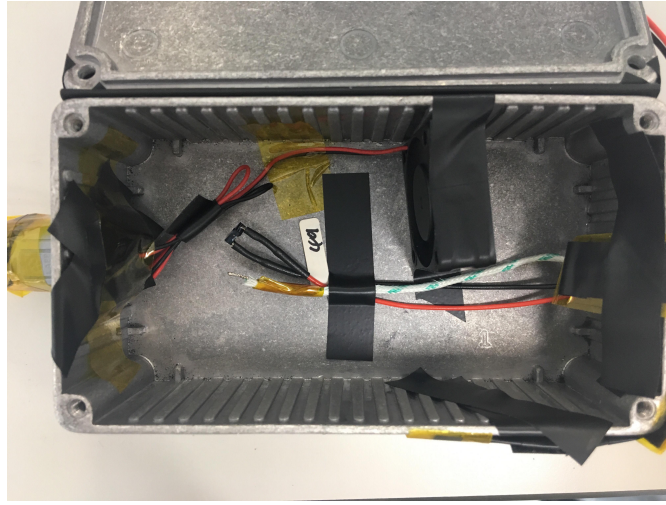


Figure 7: Picture of the inside of the aluminium box.

I-V curve meant that any change in temperature throughout the data taking was significantly reduced. This meant that the same temperature could be applied to the whole sweep, as opposed to individual temperatures for each point.

Figure 8 shows a reverse biased I-V curve for a photodiode, taken using the I-V sweep program as outlined above. It can be seen that the magnitude of the leakage current is very small, up until breakdown voltage is reached. At this point, the magnitude of the leakage current increases dramatically. I-V curves were taken on all photodiodes for two reasons: to check that the photodiode in question behaved properly, and to provide non-irradiated I-V curves for each photodiode, such that a change in leakage current before and after irradiation could be computed. All I-V curves were scaled to a reference temperature of 21°C, since room temperature measurements are recommended by RD50 [7], using equation 1. This ensured that any temperature fluctuations in the room were accounted for.

During I-V measurements, ambient sound was kept to a minimum. For a non-irradiated photodiode, at voltages with a lower magnitude than breakdown voltage, the leakage current scale was of the order of nano-amps. Due to the small currents involved, ambient noise could cause the measurement to fluctuate significantly. This made low temperature measurements challenging, because as described in section 2.2, the lower the temperature, the lower the magnitude of the output leakage current for a given voltage.

In order to test the relation as shown by equation 1, various I-V sweeps were taken at varying temperatures using an environmental chamber. The temperature range chosen was -20°C to 60°C in 5°C increments, starting from -20°C . For temperatures less than or equal to 15°C , gaseous nitrogen was pumped into the chamber at a constant rate, in order to reduce humidity and prevent

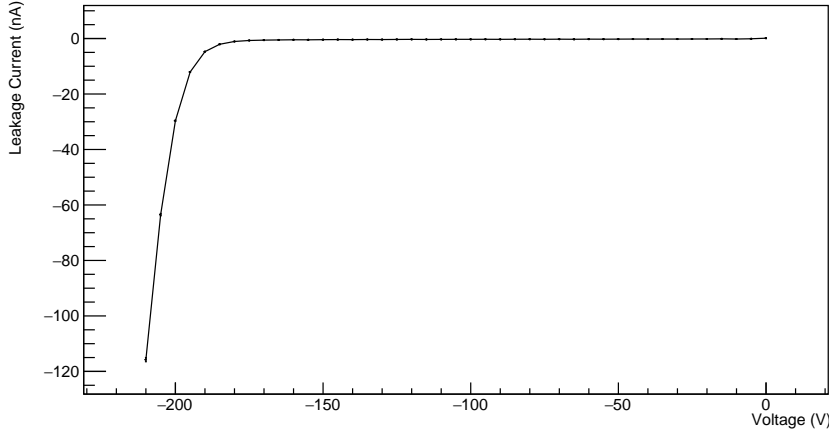


Figure 8: I–V curve for a non-irradiated photodiode.

any condensation. Due to the setup of the environmental chamber, this meant that the aluminium box and the gaseous nitrogen could not be utilised simultaneously. Therefore, the photodiode was placed within the environmental chamber with the thermocouple, with little shielding. This meant that the photodiode was susceptible to electromagnetic radiation. A 12 V fan, set to 10 V, was used within the chamber, to aid in air circulation. A bigger fan was used than the one present within the aluminium box, purely because the volume that required air circulation was bigger.

As with the standard I–V measurements, the system was then connected to the Keithley 2410 source meter, and I–V sweeps were taken. Excluding the ratio to reference temperature, equation 1 can be written as shown by equation 10.

$$I(T) = AT^2 e^{-\frac{E_a}{2k_B T}} \quad (10)$$

Where A is a constant of proportionality. Rearranging this into a $y = mx + c$ format, equation 11 can be obtained.

$$\ln\left(\frac{I}{T^2}\right) = -\frac{E_a}{2k_B} \frac{1}{T} + B \quad (11)$$

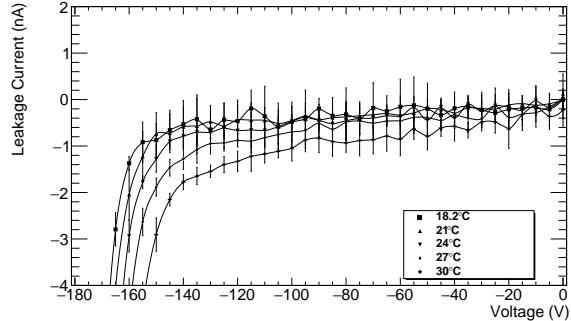
Where B is a constant derived from A . Therefore, by taking I–V curves at various temperatures using the environmental chamber, and evaluating each curve at the maximum depletion voltage in accordance with RD50 guidelines [7], which was taken to be -91 V (see section 4.2), $\ln\left(\frac{I}{T^2}\right)$ was plotted against $\frac{1}{T}$, to give a straight line graph, with the gradient being related to the activation energy of silicon. Section 6.1 outlines how the evaluation at maximum depletion voltage was undertaken.

The evaluation was done at maximum depletion voltage due to the varying size of the depletion region within the photodiode. By ensuring that the depletion region was at it's largest size when the measurement was taken, the variable of a changing depletion region was removed.

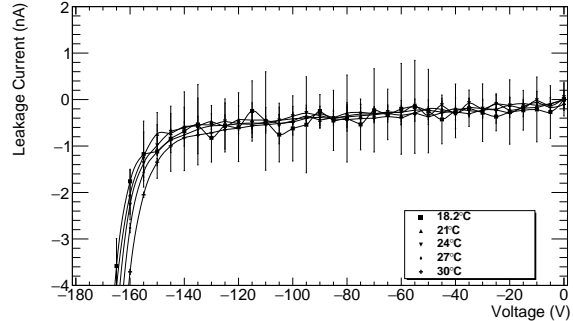
3.2 Pre-Irradiation Results

Figure 9 shows how the I–V curves were scaled such that they show the equivalent I–V curve for a reference temperature of 21°C. The errors for figure 9a were computed by taking the range divided by two of the five leakage current measurements for each voltage, outlined in section 3.1. For figure 9b, the error due to the uncertainty on the temperature (see appendix A) was added in quadrature with this, in order to obtain an overall error. It is worth noting that the y-axis ranges have been reduced to give a zooming effect.

It can be seen by figure 9, that the temperature scaling caused the various curves to line up effectively. There was some deviation in the leakage current beyond breakdown voltage, but it is theorised that this was due to immeasurable internal heating. However, this effect does not occur before breakdown voltage, and so was not an issue for this project.



(a) Non-temperature scaled I–V curve for a non-irradiated photodiode.



(b) Temperature Scaled I–V curve for a non-irradiated photodiode.

Figure 9: The effect of temperature scaling on I–V curves, taken at various temperatures.

By applying equation 11 over the temperature range as stated in section 3.1, figure 10 was obtained. Under inspection, there are 3 distinct regions. At temperatures less than $\sim 5^\circ\text{C}$, ambient noise became a major problem, due to the lower leakage current output. This therefore increased the fractional errors, meaning that this region was too noisy to give a reliable result. Due to the increasing leakage current as the temperature was increased, noise became less of a problem at higher temperatures. The gradients of the $5^\circ\text{C} \leq T \leq 30^\circ\text{C}$ (lower) and $30^\circ\text{C} \leq T \leq 60^\circ\text{C}$ (upper) linear fits are $(-6.86 \pm 2.88) \times 10^3 \text{ K}$ and $(-1.29 \pm 0.02) \times 10^4 \text{ K}$ respectively, which yield activation energy values of $E_a^{lower} = 1.18 \pm 0.50 \text{ eV}$ and $E_a^{upper} = 2.22 \pm 0.05 \text{ eV}$. Despite the large

error on E_a^{lower} , the two values are not in agreement, meaning that the range of temperatures used had an effect on the activation energy.

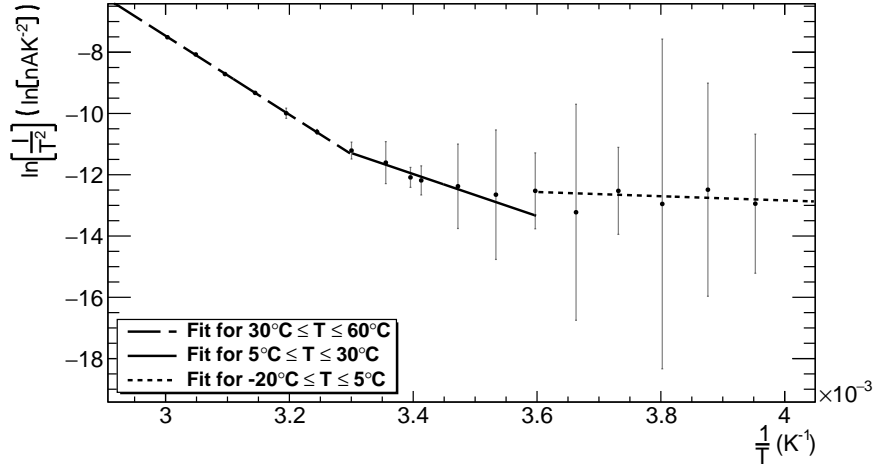


Figure 10: $\ln\left(\frac{I}{T^2}\right)$ vs $\frac{1}{T}$ for a non-irradiated photodiode, where $-20^\circ\text{C} \leq T \leq 60^\circ\text{C}$.

Since the temperature range of interest for this project was at and around room temperature, the temperature range $15^\circ\text{C} \leq T \leq 30^\circ\text{C}$ was investigated further. Due to the large errors displayed by figure 10, an investigation was done to reduce these errors. It was found that using shorter wires to connect the photodiode to the Keithley significantly reduced the errors, since the wires used previously were impractically long. Another source of error was due to the absence of the aluminium box. As predicted in section 3.1, this made the photodiode more susceptible to EM radiation. Since temperatures requiring an input flow of nitrogen were excluded, the aluminium box was reintroduced. Following this, the experiment was redone with shorter wires, and including the aluminium box, over the range specified above.

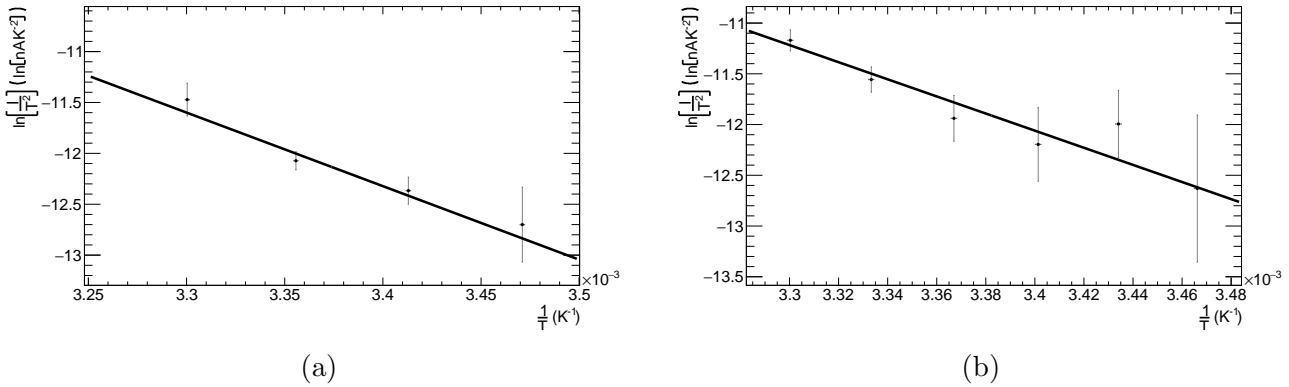


Figure 11: $\ln\left(\frac{I}{T^2}\right)$ vs $\frac{1}{T}$ for a non-irradiated photodiode, where $15^\circ\text{C} \leq T \leq 30^\circ\text{C}$.

Figure 11 shows the results. Two experiments were done on different days, with the only difference being the temperature increment. Figure 11a utilised an increment of 5°C , and figure 11b utilised an increment of 3°C , in order to obtain more points. The gradients of the fits for figures 11a and 11b were $(-7.23 \pm 1.61) \times 10^3 \text{ K}$ and $(-8.43 \pm 1.89) \times 10^3 \text{ K}$ respectively. The corresponding activation energy values were $E_a^{(a)} = 1.25 \pm 0.28 \text{ eV}$ and $E_a^{(b)} = 1.45 \pm 0.33 \text{ eV}$. Both of which were concordant with each other, and the accepted value of $E_a = 1.21 \text{ eV}$ [14], to within one standard deviation. It is also worth noting that although the error was large, it was significantly less than the error on the value as derived from figure 10. Therefore, based on this verification, a value of $E_a = 1.21 \text{ eV}$ was used for all I–V curve temperature scaling.

4 C–V Measurements

4.1 C–V Procedure

Figure 12 shows the setup used to take C–V measurements. The photodiode was placed within the same aluminium box as with the I–V measurements, for the same reasons. A thermocouple was not used for C–V measurements, since the capacitance of a photodiode in this case did not depend on its temperature. However, the 5v fan was still utilised for consistency. This meant that any unobservable effect due to the fan was kept consistent throughout measurements. The photodiode was then connected to a junction box, consisting of a set of resistors and capacitors, to prevent overloading. The Keithley 2410 source meter was connected to the junction box such that a reverse bias could be applied across the photodiode. A Wayne-Kerr component analyser was connected to the junction box via four coaxial cables. This then applied an AC voltage across the photodiode, which was used to measure the complex impedance of the system, and therefore compute an accurate measure of the capacitance.

Due to the extremely low capacitance values involved, which were of the order of pico-farads, it was found that unwanted capacitance in the circuit would have a non-negligible effect on the measurements. Simple actions such as moving the wires could change the reading (see appendix C). Because of this, the wires in the system were fixed to the desk with tape, and the four coaxial cables were kept as far apart as possible, in order to reduce any interference. On top of this, the Wayne-Kerr ‘trimming’ function was utilised: the photodiode was removed from the system, and everything else was kept the same. The circuit was then trimmed in order to take account of any capacitance in the remaining circuit. Using this, C–V curves could be taken with a relatively low error.

For the measurements themselves, the readings were taken manually from the Wayne-Kerr itself. For each voltage, three readings were taken and averaged. As with the I–V measurements,

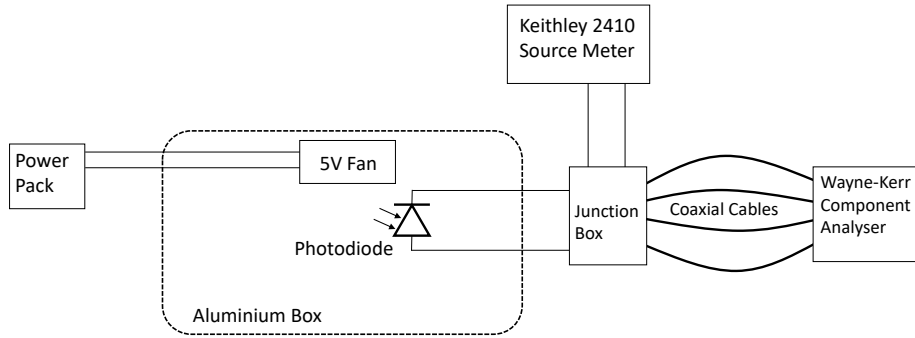


Figure 12: Schematic diagram of C–V setup.

the error on the average was taken as half of the range of readings. Referring to equation 2, up to maximum depletion voltage, capacitance is inversely proportional to the square root of the applied reverse bias. Therefore, applying similar logic as with section 3.1, equation 2 can be rearranged into a $y = mx + c$ format, as shown by equation 12.

$$\ln C = -\frac{1}{2} \ln V + D \quad (12)$$

Where D is a constant derived from the constants as described in equation 2. However, as stated in section 2.3, after maximum depletion voltage, capacitance becomes independent of voltage. Therefore, plotting $\ln C$ vs $\ln V$ should show a straight line plot, with a deviation from this at maximum depletion voltage. This procedure was undertaken for both irradiated and non-irradiated photodiodes, and the two cases were compared.

4.2 Determination of the Maximum Depletion Voltage

Figure 13 shows a C–V curve for a non-irradiated photodiode, with natural log scales, and the chosen AC frequency was 10 kHz, in accordance with RD50 guidelines [7]. As predicted, the plot displays a straight line with some deviation at higher magnitude voltages. The two regions were fit with a first order polynomial as shown by figure 13a. The fit parameters were $p_0 = 3.507 \pm 0.003$ and $p_1 = -0.3670 \pm 0.0009$ for the straight line region, and $p_0 = 2.20 \pm 0.01$ and $p_1 = (-9.92 \pm 0.21) \times 10^{-2}$ for the deviated region. As shown by figure 13b, the intersect of the two fits was found, which revealed the point on the x-axis at which the graph deviated from a straight line plot. By converting this into a voltage, the maximum depletion voltage, or the voltage at which equation 2 no longer applies could be calculated. This value was found to be $V_{max} = -90.8 \pm 5.1$ V. Therefore, all I–V curves were evaluated at a voltage value of -91 V, in order to obtain a leakage current value for each photodiode.

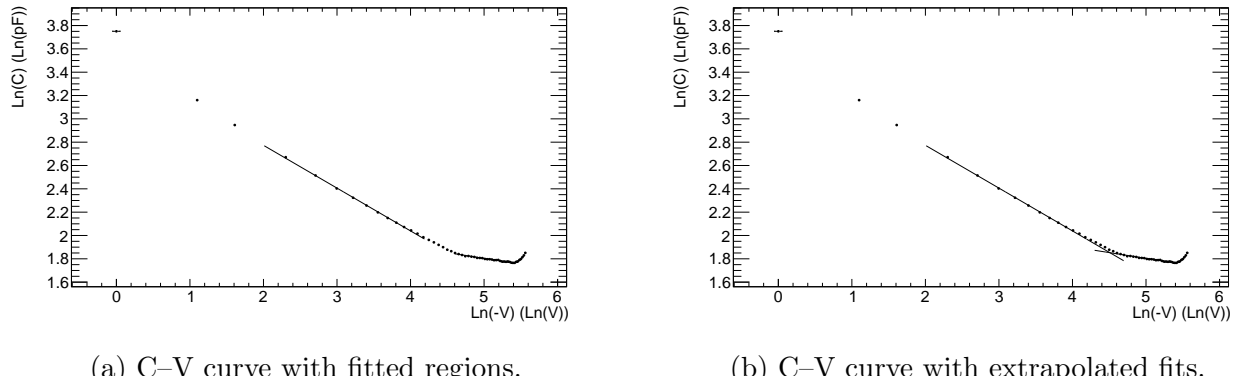


Figure 13: Natural log C–V curve for a non-irradiated diode, showing the raw fits (a), and the extrapolated fits (b), with the point of intersection.

The cause of the increase in capacitance towards the end of the deviated region is theorised to be due to the breakdown voltage of the photodiode. When the photodiode breaks down, and current flows readily, any build up of charge due to the depletion region may be allowed to dissipate, reducing the size of the depletion region, and hence increasing the capacitance. For the purposes of this project, this region was simply omitted from the fit, and no further investigation was done into this phenomenon. At lower voltages, there was a slight deviation from a straight line fit, hence why the first three points were omitted from the fit. This is most likely due to the noise floor of the Keithley having a greater effect at lower magnitude voltages and therefore currents, as explained in section 3.1.

4.3 Maximum Depletion Voltage Variation with Proton Fluence

Applying the method outlined in section 4.2 to a series of irradiated photodiodes, as well as an irradiated photodiode from KIT (see section 6.2), figure 14 was obtained. It can be seen that the magnitude of the maximum depletion voltage decreases with fluence, perhaps asymptotically. This suggests that as the degree of radiation damage is increased, either the maximum size in which the depletion region grows decreases, or the rate of growth of the depletion region with voltage increases, up to a point. Considering this, the voltage at which the photodiodes, both irradiated and non irradiated, were evaluated was kept as -91 V. The reason for this was that as long as the magnitude of the evaluation voltage was equal to or greater than the magnitude of the maximum depletion voltage, the size of the depletion region was constant. Hence, the fact that the magnitude of the maximum depletion voltage decreased with fluence did not present any obvious problems.

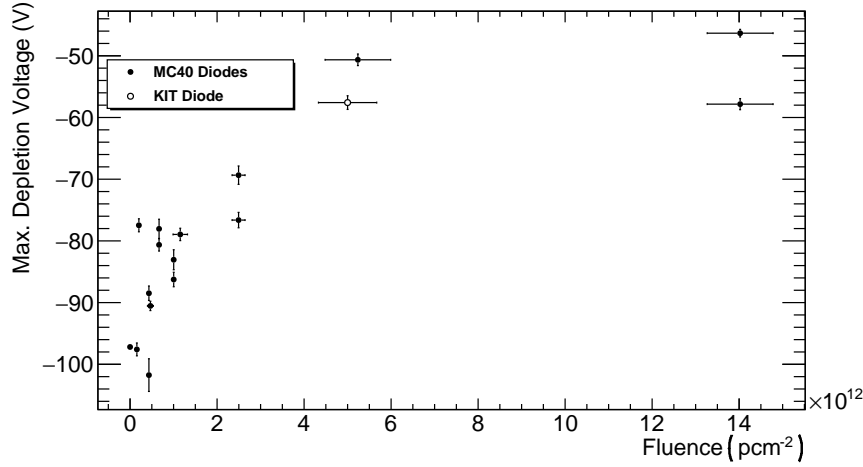


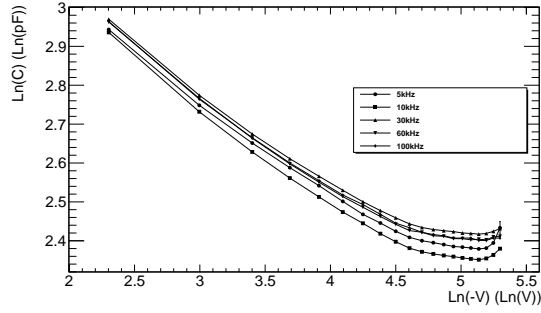
Figure 14: Maximum depletion voltage vs proton fluence for both the MC40 cyclotron photodiodes and the KIT photodiode.

4.4 Frequency Dependence of Capacitance

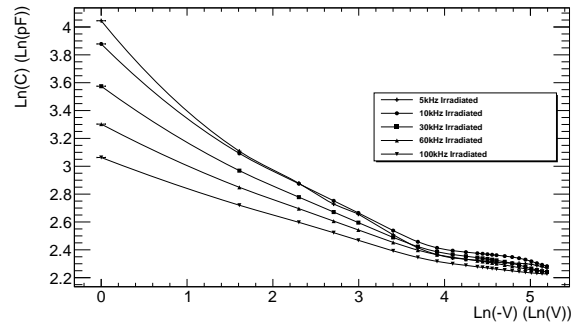
The radiation damage induced processes as described in section 2.4 each have a different lifetime, and so the rate of charge contribution varies for different processes. Depending on the frequency of the AC voltage, the lifetime of a particular process may be too short for it to contribute any charge to the system, meaning that by varying the AC frequency and taking the corresponding C–V curve, the various processes can be separated out. The lower the frequency, the more processes have time to contribute charge, and hence the higher the measured capacitance. However, this should not effect the size of the depletion region, and so the maximum depletion voltage should be independent of AC frequency.

By utilising the setup as outlined in section 4.1, C–V curves were taken for 5 kHz, 10 kHz, 30 kHz, 60 kHz, 100 kHz AC frequencies, for both an irradiated and non-irradiated photodiode.

As shown by figure 15a, changing the applied AC frequency has little effect on the capacitance of a non-irradiated photodiode. However, as shown by figure 15b, the capacitance drastically changes with the applied AC frequency. As expected, the lower frequencies produced a higher capacitance, and there was no significant change in the maximum depletion voltage (see appendix B).



(a) Non-irradiated C–V curve variation with frequency.



(b) Irradiated C–V curve variation with frequency. The photodiode was irradiated to $5.2 \times 10^{12} \text{ pc m}^{-2}$.

Figure 15: Natural log C–V curves at varying AC frequency.

5 Proton Irradiations

5.1 Irradiation Procedure

For all proton irradiations, the ATLAS chamber at the MC40 cyclotron was utilised. The initial beam energy for this project was 28 MeV, which gave a beam energy of ~ 25 MeV on the actual photodiodes. This was determined by Geant4 simulations, as shown by figure 16, which simulates the loss in beam energy as it traverses through obstacles between the end of the beam pipe and the photodiodes.

For environmental control during irradiations, a polystyrene lined isolation box was utilised. Figure 17a shows an image of this. The beam direction was out of the page, traversing through the isolation box lengthways and impacting a Faraday cup, shown on the left side of the image. The purpose of the Faraday cup was to measure the beam current, which could then be used to provide an estimate of how long the beam needed to be run in order to achieve a desired fluence, as shown by equation 13.

$$\begin{aligned} I_{beam} &= \frac{dq}{dt} \Rightarrow n_p = \frac{I_{beam}}{q_e} \\ t &= \frac{F}{n_p} = \frac{F q_e}{I_{beam}} \end{aligned} \quad (13)$$

Where t is the run time, F is the desired fluence, n_p is the number of protons per second incident on the Faraday cup, q_e is the electron charge, and I_{beam} is the current measured on the Faraday cup, which was set to 1 nA. The Faraday cup could measure beam currents of the order

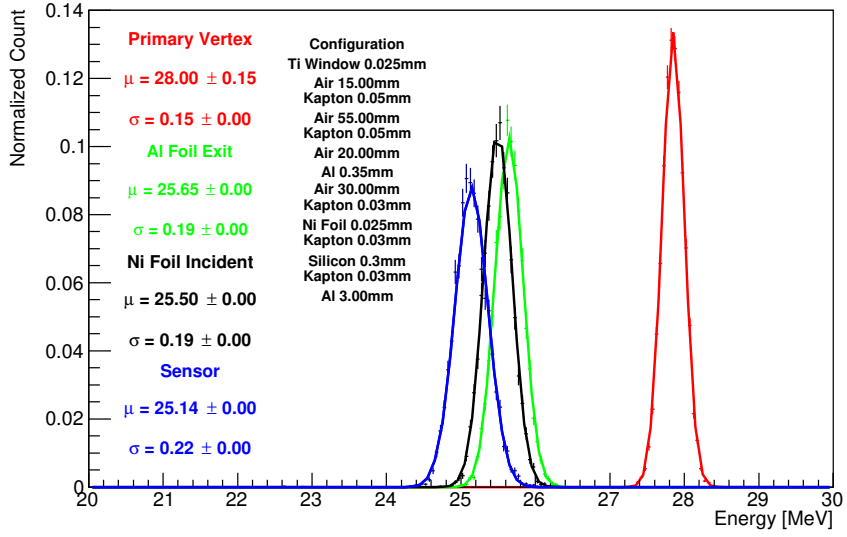


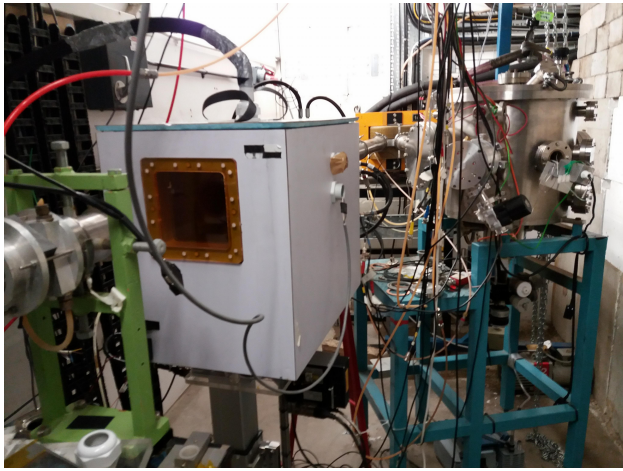
Figure 16: Geant4 simulation revealing the incident beam energy, the energy at the nickel foils, and the energy at the photodiodes (Courtesy of Dr. T. Price).

of nano-amps [15], which therefore limited the minimum fluence that can be applied. Figure 17b shows an image of inside the isolation box. In this case, the beam is traversing from right to left. The aluminium mount used to contain the photodiodes was placed behind a $450\ \mu\text{m}$ thick aluminium plate in order to block any low energy protons within the beam.

Figure 18 shows how the photodiodes were mounted on the aluminium plate, where the beam direction is into the page. Due to its radiation resistant nature, kapton tape was used. Figure 18a shows each individual photodiode position. The photodiodes were organised into pairs, such that each pair could fit within the beam profile. Hence, each position could be irradiated to a different fluence, giving a total of six fluences, with two photodiodes at each fluence.

Figure 18b shows the same mount, but with nickel foils attached to the front of each photodiode position. The nickel foils were used to obtain an accurate measure of the incident fluence through each position (see section 5.3).

After the preliminary run, two main irradiation runs were undertaken: a ‘cold’ run, involving twelve photodiodes, and a room temperature run, involving ten photodiodes. The reason for the differing temperature was to check the effects of annealing due to irradiation. Fluences ranging from $2 \times 10^{11}\ \text{pcm}^{-2}$ to $6 \times 10^{12}\ \text{pcm}^{-2}$ were chosen. The reason for this chosen range was that these fluences were not so low such that the Faraday cup became unreliable, but no so high such that the relation between the change in leakage current and fluence described by equation 6 became non-linear (see section 6.2). The irradiations were undertaken in order of highest fluence to lowest



(a) Picture of the ATLAS chamber.



(b) Picture of inside the isolation box.

Figure 17: The isolation box within the ATLAS chamber at the MC40 cyclotron.

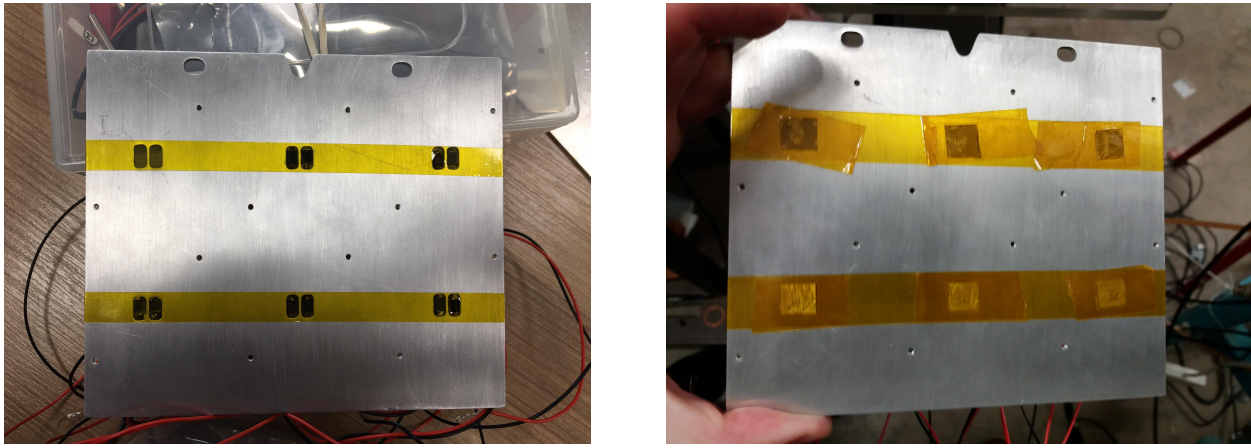
fluence. This was due to the counts signal from the nickel foils being stronger at higher fluences, so any decay in that signal over time did not have as much of an effect on the measurement as a decay in the signal of a lower fluence nickel foil.

For the room temperature irradiations, the temperature within the isolation box was uncontrolled, which meant that any heating due to irradiation could have an effect. For the ‘cold’ temperature run, gaseous nitrogen was pumped into the isolation box to reduce the humidity to $< 10\%$. Liquid nitrogen was then used to reduce the temperature in the box to -27°C . The reason for the reduction in humidity was, as with the I–V measurements, simply to prevent any condensation forming within the isolation box. After irradiations, the photodiodes and nickel foils were removed from the aluminium mount, the photodiodes were placed into a freezer to prevent any annealing, and the nickel foils were measured in order to obtain the fluence for each position. For the ‘cold’ temperature run, after irradiations the system was left for two hours in order to equalise with room temperature.

5.2 Beam Calibration

In order to irradiate six distinct positions separately, as shown by figure 18, the beam position relative to the mount was moved. Since moving the beam line itself was impractical, the isolation box with the photodiodes was moved around the beam line with the use of a robot, controlled by using a co-ordinate system in labVIEW.

An identical aluminium mount was covered with gafchromic film, which changes colour when radiation is incident on its surface. The isolation box was moved to its ‘home’ position, and the



(a) Photodiode cyclotron mount without the nickel foils.

(b) Photodiode cyclotron mount with included nickel foils.

Figure 18: Aluminium mount used for proton irradiations.

beam was run through the film. The position of the beam on the film was then measured as a function of distance from each photodiode position, such that the coordinates of each position with respect to the beam could be calculated. The film was then irradiated at each of these positions to check the alignment of the beam.

5.3 Nickel Foil Activation

By analysing the $^{nat}Ni(p, x)^{57}Ni$ 1377 keV peak after irradiation, an accurate measure of the incident fluence for each photodiode position could be determined.

Using Maestro, the net number of counts was measured over 500s live time using a germanium counter: starting from the highest fluence foil and working down to the lowest fluence foil, for reasons explained in section 5.1. A preset spreadsheet [16] was used to convert the measured counts to a corresponding proton fluence, based on the time between irradiation and measurement, the live time, the foil weight, and the foil area. The foil weight and area were looked up using a given catalogue [17].

Figure 19 displays the setup used for the nickel foil activation. The ‘calibrated position’ refers to the position above the counter for which the preset spreadsheet was calibrated. However, the activity of the foils was too low to achieve a good measurement of the counts at the calibrated position. Hence, the nickel foils were placed directly on the counter, or the ‘counter position’, in order to get a stronger reading. The fluences obtained through this were therefore larger than the true values. Hence, a calibration factor, which was the ratio of fluences of the ‘counter position’ to the ‘calibrated position’, was used to convert the obtained fluences to the actual fluences.

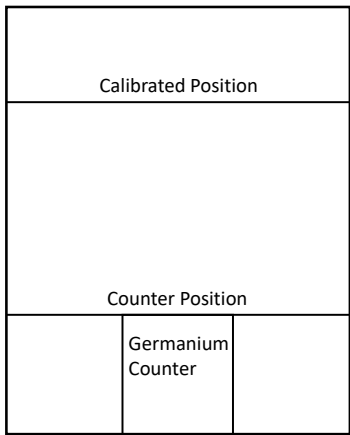


Figure 19: Schematic diagram of the germanium counter.

The calibration factor was initially calculated by taking the highest activity nickel foil, and computing the fluence at each position, as displayed in figure 19. The ratio of the two fluences was then taken. However, this proved to be unreliable. Multiple experiments were done, each with varying values providing inconclusive results. Therefore, a strong cobalt-60 source was used. Cobalt-60 has two distinct gamma peaks, 1173 keV and 1332 keV [18]. The net counts for each peak were taken three times at each position. Taking the ratio of the two positions, this gave six calibration factors (see appendix D). Taking an average, the calibration factor was found to be 112.67 ± 5.91 . The error was due to the error on the counts from maestro, added in quadrature with the range of values divided by two. All fluences measured from the

counter position were then scaled back using this value to obtain the true, calibrated fluences.

5.4 Annealing Procedure

Annealing due to effects such as beam fluence, room temperature annealing, and other uncontrollable effects meant that each photodiode had an unknown degree of annealing. Calculating the change in leakage current from photodiodes in this state was therefore unreliable, as it prevented a robust comparison between different photodiodes. Hence, the thermal history of the photodiodes prior to the post-irradiation I-V measurements was removed.

This was done by further annealing the photodiodes for 80 minutes at 60°C according to RD50 guidelines [7]. Applying equation 4 to this, the equivalent degree of annealing would take several weeks at room temperature. This meant that any annealing of the photodiodes prior to the annealing procedure was essentially made completely negligible.

The annealing was also done in order to reduce the rate of further annealing. Since the annealing rate exponentially decays over time, as the photodiode repairs itself, by annealing for a sufficient amount of time, the annealing rate can be significantly reduced, therefore increasing the reliability of comparison between photodiodes. To reduce the rate of annealing further, whenever irradiated photodiodes were not being analysed, they were stored inside of a freezer at -25°C.

Figure 20 shows how the leakage current, evaluated at -91 V, of an irradiated photodiode varies with the annealing time, totalling an annealing time of 80 minutes. In order to achieve a temperature of 60°C, a preheated oven was used. Since the displayed oven temperature was

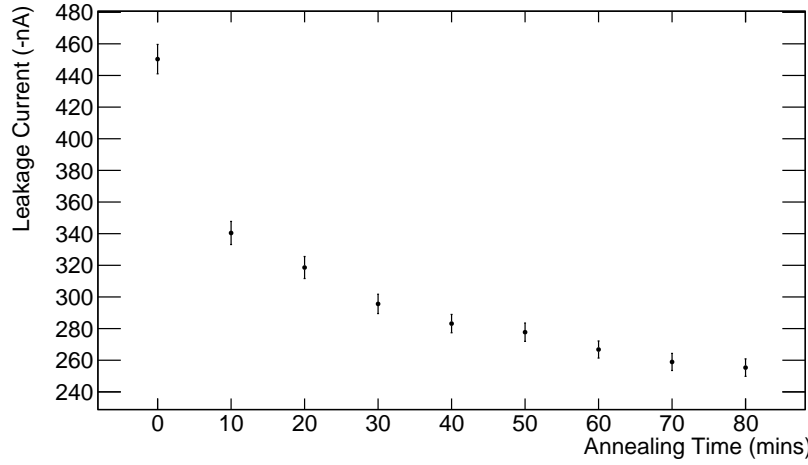


Figure 20: Leakage current vs annealing time for an irradiated photodiode. The annealing temperature was 60°C.

inaccurate, a thermocouple was placed within the oven, in order to obtain an accurate temperature reading (see appendix E).

The procedure itself started by removing the photodiode in question from the freezer and leaving it to equalise with room temperature for 15 minutes. An initial I–V curve was then taken before any annealing was undertaken. Before placing the photodiode in the oven, it was blasted with hot air from a hairdryer for 5 seconds. To ensure the air coming from the hairdryer was actually hot, it was allowed to run for 30 seconds before blasting the photodiode. After waiting 30 seconds for the oven to recover (see appendix E), the temperature was recorded. Then, after 10 minutes, the photodiode was removed from the oven after taking a final oven temperature, and blasted with cold air from the same hairdryer for 30 seconds. This was done to bring the temperature of the photodiode back down to room temperature. The reason for the flash heating and cooling with the hairdryer was to ensure that the only significant annealing of the photodiode was done with the photodiode in the oven. For example, not cooling the photodiode down after annealing would mean that it would continue annealing until the temperature dropped naturally, meaning that the photodiode would overall anneal more than intended.

After each annealing period, an I–V curve was taken, before putting the photodiode back into the oven using the same procedure as outline above. This process was repeated until a cumulative annealing time of 80 minutes had been reached.

As shown by figure 20, it can be seen that after 80 minutes of annealing, the rate of change of leakage current, and therefore the annealing rate, has become low enough such that any further change is negligible in comparison. The procedure was then implemented to all irradiated photo-

diodes, ensuring that all photodiodes had the same thermal history. The main concern with this procedure was the fluctuation in the oven temperature. The oven temperature tended to oscillate around 60°C by approximately 3°C. Over 80 minutes, this fluctuation would average out, but due to the exponential nature of the Arrhenius equation, a slight change in temperature could lead to a large change in annealing time. Equation 14 shows a rearranged version of equation 4, utilising ratios to calculate the equivalent annealing time for temperatures other than 60°C.

$$\tau = 80 \text{ mins} \times e^{-\frac{E_{anneal}}{k_B} \left(\frac{1}{60^\circ\text{C}} - \frac{1}{T} \right)} \quad (14)$$

By adopting a value of $E_{anneal} \approx 1.03$ eV [11, p. 211], and assuming that the average oven temperature deviated from 60°C by no more than 1°C, it was found that this deviation would give a change in annealing time of approximately 9 minutes. Comparing this to figure 20, this does not effect the corresponding leakage current value, within errors. Hence, the fluctuation in the oven temperature was not taken to be a major source of error, but this does require further investigation.

The pairs of photodiodes, as shown by figure 18a, were split into two sets and annealed separately in groups of six. The photodiodes were left within the oven for the full 80 minutes, in order to reduce any errors due to the oven recovery time by measuring the photodiodes every 10 minutes. The reason for the groups was to avoid any major data loss in the event of the annealing procedure failing. Furthermore, annealing in groups meant that any deviation in the annealing temperature acted as a constant error over all photodiodes in that particular set, and it therefore induced no effect on the relative thermal history between the photodiodes.

6 Determination of the Hardness Factor

6.1 MC40 Cyclotron Analysis

Figure 21 shows a series of I-V curves taken from irradiated I-V curves, post-annealing. As predicted by equation 6, the magnitude of the leakage current increases with fluence. There was some deviation at higher magnitude voltages, but this is simply due to the fact that the breakdown voltage varies slightly from photodiode to photodiode.

Like previous experiments, each I-V curve was evaluated at a maximum depletion voltage of -91 V. In order to do this, each I-V curve was fit, with a first order polynomial, over the range -110 V to -40 V for non-irradiated photodiodes, and -100 V to -75 V for irradiated photodiodes, using the ROOT data analysis framework. The reason for the range differences was that the irradiated photodiodes experienced more exaggerated I-V curves than the non-irradiated equivalents. Hence,

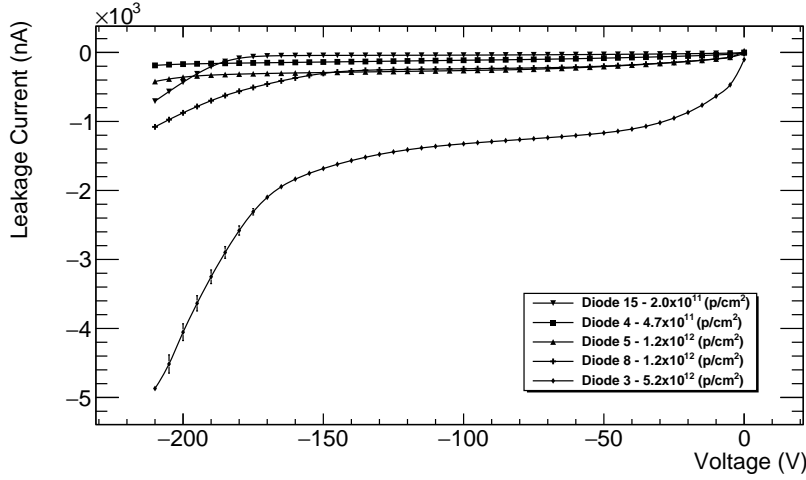


Figure 21: Post-irradiation and annealing photodiode I–V curves for varying fluences.

the range over which the curve was linear was reduced. Figure 22 shows examples of how the curves were fit, where figure 22a shows the non-irradiated case, and figure 22b shows the curve for the same photodiode, but post-irradiation and annealing.

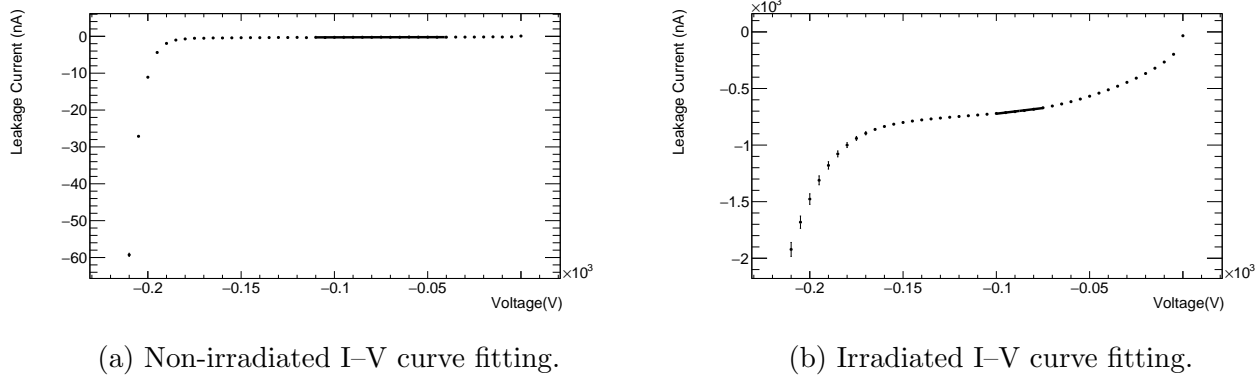


Figure 22: Example I–V curve fittings.

Each fit was then evaluated at -91 V, and the difference between the irradiated case and the non-irradiated case was taken for each photodiode, in order to obtain the change in leakage current. The change in leakage current was then plotted as a function of applied proton fluence, and fit using a first order polynomial, where the fluences were taken from the nickel foil analysis. Due to the annealing process, it was found that varying the temperature of the isolation box between irradiations had no effect on the change in leakage current. Hence, both data sets were treated as a single set.

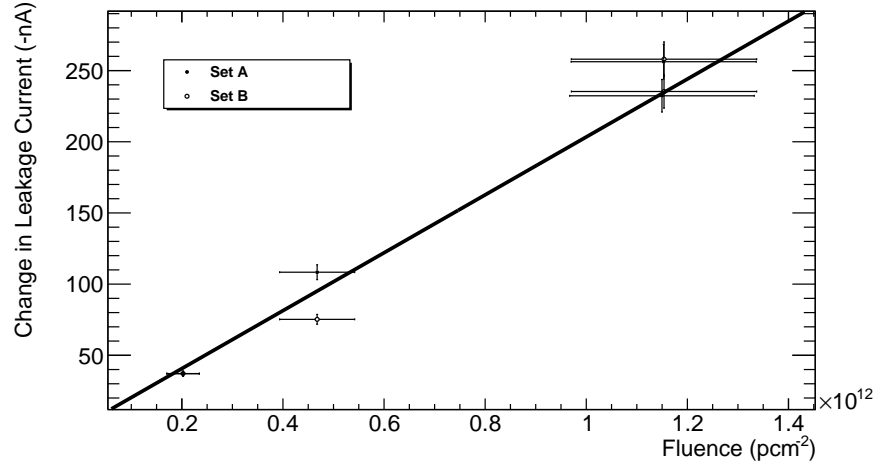


Figure 23: Change in leakage current vs proton fluence, preliminary plot, with an included linear fit.

Figure 23 shows the preliminary irradiations result. Here, the photodiodes were all irradiated at a temperature of -27°C , and ‘Set A’ and ‘Set B’ refer to the two sets of photodiodes on the aluminium mount, as explained in section 5.4. The y-intercept of the fit was set to zero due to the fact that a fluence is required to achieve a change in leakage current. Therefore, it was only logical that the plot should intersect the origin. This produced a gradient of $(2.03 \pm 0.12) \times 10^{-10} \text{ Acm}^2$. And, applying equation 6, the gradient was equal to $\alpha l^2 w$. Adopting values for $l^2 = (0.265 \times 0.265) \text{ cm}^2$ [19] and $w = 300 \mu\text{m}$ [20, p. 4], this gave a value of the current related damage rate of $\alpha = (9.65 \pm 0.57) \times 10^{-17} \text{ Acm}^{-1}$. Utilising a value of $\alpha_{neq} = (3.99 \pm 0.03) \times 10^{-17} \text{ Acm}^{-1}$ [11, p. 105], the preliminary value of the hardness factor was found to be $\kappa_{MC40}^{prelim} = 2.42 \pm 0.14$.

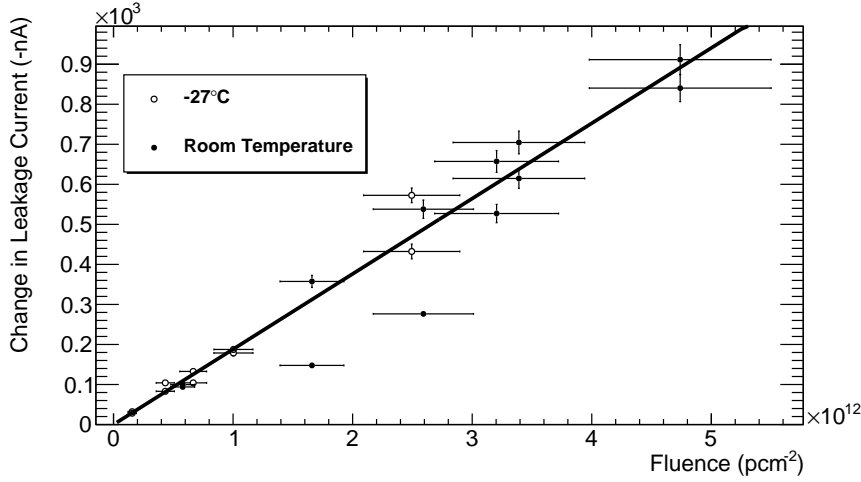


Figure 24: Change in leakage current vs proton fluence, with an included linear fit over all MC40 cyclotron data.

Figure 24 displays all twenty two photodiodes from the two main cyclotron runs on one plot. Again, the fit was forced through the origin, and the gradient of the fit was found to be $(1.88 \pm 0.07) \times 10^{-10} \text{ A cm}^2$. By adopting the same values as quoted above, the current related damage rate was found to be $(8.93 \pm 0.34) \times 10^{-17} \text{ A cm}^2$, giving a hardness factor result of $\kappa_{MC40} = 2.24 \pm 0.09$. There was some deviation in leakage current between photodiodes irradiated to the same fluence (see Appendix F), this was thought to be due to the beam profile. For example, the fluence for each position was measured by using a single nickel foil. However, each nickel foil covered two photodiodes, meaning that each photodiode could receive a slightly different fluence. Therefore, if the beam profile was asymmetric, this would not show in the nickel foil analysis, but would show in the varying leakage current for two photodiodes in the same position on the aluminium plate.

6.2 KIT Analysis

A similar procedure was undertaken on photodiodes irradiated at the Karlsruhe Institute of Technology. Table 1 shows the available fluences. As per convention, the fluences were given in the 1 MeV neutron equivalent format. Since a hardness factor of 2 was used to convert the proton fluences to the 1 MeV neutron equivalent fluences, a hardness factor of 2 was used to convert them back to proton fluences.

It is worth noting that all photodiodes except one are BPW34FS photodiodes, as opposed to BPW34F photodiodes. However, after looking up the data sheets for the two types of photodiodes [19][21], for the purposes of this project, the two photodiodes behave in the same way. Due to reasons discussed in section 5.4, the photodiodes were annealed for 80 minutes at 60°C in order to

Table 1: Table of fluences for KIT photodiodes.

Photodiode Type	Fluence (neq cm^{-2})	Fluence (p cm^{-2})
BPW34FS	1×10^{13}	5×10^{12}
BPW34FS	1×10^{14}	5×10^{13}
BPW34F	3×10^{14}	1.5×10^{14}
BPW34FS	1×10^{15}	5×10^{14}

remove any thermal history. Then, utilising the same code as for the MC40 cyclotron photodiodes, each measured I–V curve was evaluated at -91 V, and plotted as a function of proton fluence. The difference between the irradiated and non-irradiated curves was impossible to compute, simply due to the fact that the KIT photodiodes were not analysed before irradiation. However, since the difference between the leakage current of an irradiated and a non-irradiated photodiode is several orders of magnitude, the change in leakage current was approximately the same as the irradiated leakage current. Despite this, the fit was not forced through the origin, since the pre-irradiation conditions were unknown. Figure 6.2 shows the results.

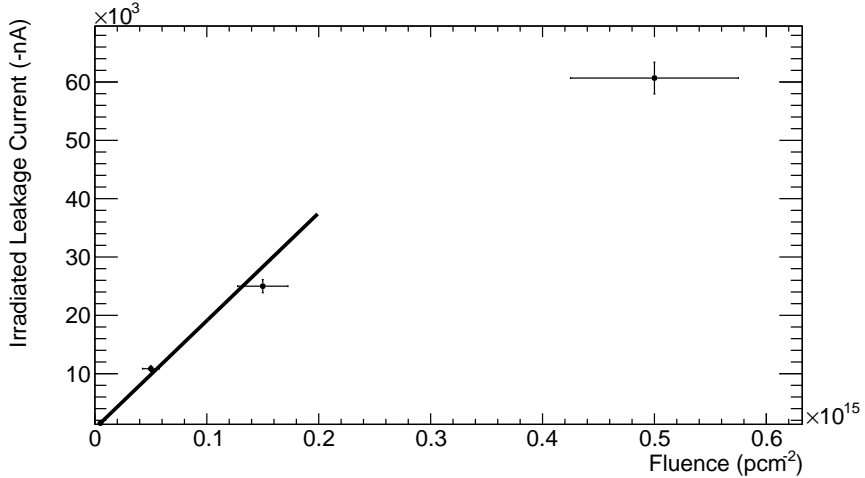


Figure 25: Change in leakage current vs proton fluence for KIT photodiodes.

The gradient of the displayed fit is $(1.85 \pm 0.22) \times 10^{-10} \text{ Acm}^2$. Using the same values as stated in section 6.1, this gave values of $\alpha = (8.77 \pm 1.06) \times 10^{-17} \text{ Acm}^{-1}$ and $\kappa_{KIT} = 2.20 \pm 0.27$. According to figure 3 in [20, p. 3], it appears that for fluences higher than $10^{13} \text{ neqcm}^{-2}$, the relationship between leakage current and incident fluence becomes non linear. The fluence range used for the MC40 cyclotron photodiodes was below this limit. However, as shown by figure 25, the fluences used for the KIT photodiodes were above this limit, and so deviate from the linear trend. As the fluence increases, the deviation becomes greater. Hence, in order to achieve a balance between

linearity and the number of points, the highest fluence was excluded from the fit, but the fluence at 1.5×10^{14} pcm^{-2} is included, despite its deviation.

7 Conclusion and Discussion

The I–V and C–V characteristics of BPW34F photodiodes have been analysed. By evaluating at a maximum depletion voltage value of -91 V, the change in leakage current before and after irradiations for each photodiode was computed. The proton fluence was determined by measuring the net counts of the 1377 keV peak of irradiated nickel foils, and converting it to proton fluence. By plotting the change in leakage current vs the proton fluence, a current related damage rate of $\alpha = (8.93 \pm 0.34) \times 10^{-17}$ Acm^{-1} was inferred. This in turn gave a value of $\kappa_{MC40} = 2.24 \pm 0.09$ for 25 MeV protons, which agrees with the preliminary measurement of $\kappa_{MC40}^{prelim} = 2.42 \pm 0.14$, the currently used value of 2.2, and the previously quoted value of 2.05 ± 0.61 for KIT. Comparing to the previously obtained value of 1.64 ± 0.27 however, there is a discrepancy. Applying a similar method to photodiodes irradiated at KIT, a current related damage rate value of $\alpha = (8.77 \pm 1.06) \times 10^{-17}$ Acm^{-1} was inferred, which gave a corresponding hardness factor value of $\kappa_{KIT} = 2.20 \pm 0.27$ for 24 MeV protons. This value agrees with the MC40 value to within one standard deviation.

In terms of issues with this project, there were three main problems. The first issue was that the beam profile was not perfect: this meant that two photodiodes in the same position could receive different fluences, but the same fluence for both would be recorded. The second issue was with the fluctuating oven temperature during the annealing procedure: although the fluctuations would average out over time, small deviations in the average temperature could lead to a large deviation in the annealing time. Hence, future tests should be done on how the oven fluctuates, and whether or not this has any effect on the average annealing temperature. The third issue was with the calibration factor during the nickel foil analysis: this problem was eventually solved with the use of a strong cobalt-60 source, but the experiment was never repeated, and so further experiments should be done in order to validate the obtained value.

For the future of this project, collaborations with IRRAD could yield a more independent result for the hardness factor. IRRAD irradiates at room temperature, with a 24 GeV proton beam, which is three orders of magnitude higher than the MC40 cyclotron. Since during this project it was found that irradiating at room temperature is essentially the same as irradiating at -27°C (after annealing), calculating the ratio of gradients of a change in leakage current vs proton fluence plot for the two different energies, would show how the hardness factor varies with beam energy. Furthermore, continued collaborations with KIT by comparing more photodiodes irradiated to the same fluence as the MC40 photodiodes, would aid in reinforcing the value of the hardness factor obtained for the MC40 cyclotron.

References

- [1] ATLAS Collaboration. *Letter of Intent for the Phase-II Upgrade of the ATLAS Experiment*. 2012. URL: <http://cds.cern.ch/record/1502664>.
- [2] T. Price. *Experimental Determination of the Hardness Factor for the Birmingham Irradiation Facility*. June 2017. URL: <https://indico.cern.ch/event/637212/contributions/2608664/>.
- [3] A. Dierlamm. *Proton Irradiation in Karlsruhe*. 16th RD50 Workshop. 2010. URL: https://indico.cern.ch/event/86625/contributions/2103519/attachments/1080676/1541436/Irradiations_Ka.pdf.
- [4] R. Canavan. “Using the Radiation Damage of Silicon Photodiodes to Determine the Hardness Factor of the MC40 Cyclotron”. In: (2017). Masters report, University of Birmingham.
- [5] P. Knights. “Measurement of the Hardness Factor for Proton Irradiations”. In: (2017). Masters report, University of Birmingham.
- [6] M Moll et al. “Relation between microscopic defects and macroscopic changes in silicon detector properties after hadron irradiation”. In: *Nuclear Instruments and Methods in Physics Research Section B: Beam Interactions with Materials and Atoms* 186.1 (2002), pp. 100–110. ISSN: 0168-583X. DOI: [https://doi.org/10.1016/S0168-583X\(01\)00866-7](https://doi.org/10.1016/S0168-583X(01)00866-7). URL: <http://www.sciencedirect.com/science/article/pii/S0168583X01008667>.
- [7] RD50. Mar. 2018. URL: <http://rd50.web.cern.ch/rd50/>.
- [8] R. Nave. *Fermi Level and Fermi Function*. Mar. 2018. URL: <http://hyperphysics.phy-astr.gsu.edu/hbase/Solids/Fermi.html>.
- [9] Brian K. Tanner. *Introduction to the Physics of Electrons in Solids*. Cambridge University Press, 1996.
- [10] P-N Energy Bands. Mar. 2018. URL: <http://hyperphysics.phy-astr.gsu.edu/hbase/Solids/pnjun2.html>.
- [11] M. Moll. “Radiation Damage in Silicon Particle Detectors”. PhD thesis. University of Hamburg, 1999.
- [12] G. Casse. “The effect of hadron irradiation on the electrical properties of particle detectors made from various silicon materials”. PhD thesis. Universite Joseph Fourier-Grenoble, 1998.
- [13] H. M. Rosenberg. *The Solid State, 3rd Edition*. Oxford Science Publications, 2006.

- [14] A Chilingarov. “Temperature dependence of the current generated in Si bulk”. In: *Journal of Instrumentation* 8.10 (2013), P10003. URL: <http://stacks.iop.org/1748-0221/8/i=10/a=P10003>.
- [15] Willi A. Brand Michael E. Wieser. “Isotope Ratio Studies Using Mass Spectrometry”. In: *Encyclopedia of Spectroscopy and Spectrometry (Second Edition)* (1999).
- [16] BILPA. *Birmingham Irradiations TWiki*. file: *new_Ni_May16 – lg.xlsx*. Mar. 2018. URL: <http://www.ep.ph.bham.ac.uk/twiki/bin/view/BILPA/BhamIrrad>.
- [17] BILPA. *Birmingham Irradiations TWiki*. file: *Ni – foils – L – weight.pdf*. Mar. 2018. URL: <http://www.ep.ph.bham.ac.uk/twiki/bin/view/BILPA/BhamIrrad>.
- [18] NNDC. ^{60}Co Decay Radiation. Mar. 2018. URL: <https://www.nndc.bnl.gov/chart/decaysearchdirect.jsp?nuc=60CO&unc=nds>.
- [19] OSRAM opto semiconductors. *Silicon PIN Photodiode with Daylight Blocking Filter Version 1.5: BPW34F*. Apr. 2016. URL: https://www.marutsu.co.jp/contents/shop/marutsu/ds/00215978_0.pdf.
- [20] F. Ravotti et al. *BPW34 Commercial p-i-n Diodes for High-level 1-MeV Neutron Equivalent Fluence Monitoring*. IEEE, 2007.
- [21] OSRAM opto semiconductors. *Silicon PIN Photodiode with Daylight Blocking Filter Version 1.1: BPW34FS*. Jan. 2014. URL: http://www.produktinfo.conrad.com/datenblaetter/150000-174999/153057-da-01-ml-PIN_PHOTODIODE_BPW34FS_de_en.pdf.
- [22] F. S. Al Saleh et al. “Excitation Functions of (p,x) Reactions on Natural Nickel Between Proton Energies of 2.7 and 27.5 MeV”. In: *Applied Radiation and Isotopes* 65 (May 2007).

Appendices

A Justification of Errors

All error propagation was done by utilising the general error equation for a function $f(x_1, x_2, \dots, x_n)$, as shown by equation 15.

$$\sigma f(x_1, x_2, \dots, x_n) = \sqrt{\sum_{i=1}^n \left[\frac{\partial f}{\partial x_i} \sigma x_i \right]^2} \quad (15)$$

The raw errors were estimated as follows:

- 0.05 V apparatus error on the applied voltage of the Keithley 2410 source meter.
- 0.1°C error on the temperature of each I–V curve, determined by taking the average of the temperature change during several I–V sweeps, and halving it.
- The current for a particular voltage was determined by taking five values and averaging them. Therefore the error was taken as half of the range of these values.
- The apparatus error of the measured current from the Keithley was not included, as it was negligible next to the current fluctuation.
- The capacitance for a particular voltage was determined by taking three values and averaging them. Therefore, as with the current, the error was taken as half of the range of these values.
- Apparatus error of the Wayne-Kerr, determined by the number of decimal places of the measurement, which changed as the capacitance changed. For example, if there were three decimal places present, then the error would be taken as 0.0005. This was included due to the fact that it was non negligible next to the capacitance fluctuation.
- The error due to the counts of the measured nickel foils. Taken from the 1377 keV peak in MAESTRO.
- Half of the range of calibration factors for the cobalt-60 calibration.
- Related to measured fluence, 15.9% error due to the uncertainty on the $^{nat}Ni(p, x)^{57}Ni$ cross section, which was taken to be 170 ± 27 mb for 25 MeV protons [22, p. 107].
- Estimated 15% error on the KIT fluences, based on a comparison with the errors for the MC40 fluences.

These errors were propagated through the analysis code where necessary, and so they contributed to any errors on fits.

B Maximum Depletion Voltage Relation to AC Frequency

Multiple C–V curves for the same photodiode, but at different AC frequencies were analysed to determine whether or not the maximum depletion voltage varies with frequency. The experiment was done on both an irradiated and non-irradiated photodiode, using the same procedure as outlined in section 4.2. Table 2 shows the results.

Table 2: Maximum depletion voltage variation with AC frequency.

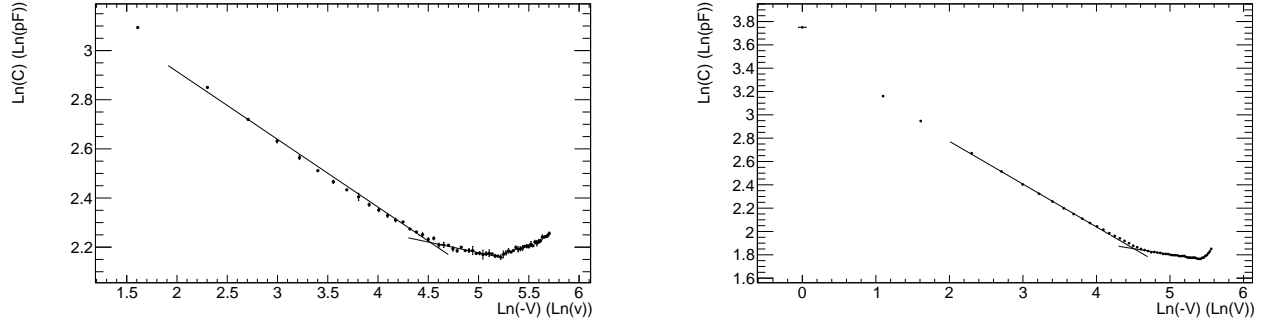
Irradiated to 5.23×10^{12} pcm^{-2}	
AC Frequency (kHz)	Max. Depletion Voltage (V)
5	-46.8 ± 4.2
10	-42.5 ± 2.2
30	-39.0 ± 3.5
60	-41.4 ± 13.5
100	-45.6 ± 1.7

Non-Irradiated	
AC Frequency (kHz)	Max. Depletion Voltage (V)
5	-94.1 ± 7.9
10	-97.2 ± 4.0
30	-95.7 ± 5.1
60	-100.2 ± 4.5
100	-98.5 ± 6.5

It can be seen that within the error, the maximum depletion voltage does not depend on the applied AC frequency. Here, the errors are determined by the errors on the fit parameters.

C C–V Error Optimisation

Figure 26 shows two C–V curves before and after the errors were optimised. It was found that the capacitance in the wires was changing the measurement. Furthermore, the close proximity of the wires connecting the Wayne-Kerr to the junction box meant that capacitance within the circuit was increasing the error of the experiment.



(a) C–V curve for a non-irradiated photodiode before error optimisation.

(b) C–V curve for a non-irradiated photodiode after error optimisation.

Figure 26: C–V curves before and after irradiation.

By using the same method as outlined in section 4.2, the maximum depletion voltage for figure 26a was found to be -92 ± 23 V. The large error associated with this measurement meant that the value was impractical. Hence, the setup was rearranged to the setup as shown by figure 12. This improved the value of maximum depletion voltage to -90.8 ± 5.1 V (from figure 26b), as quoted in section 4.2.

D Cobalt-60 Calibration

Table 3 shows the calculated calibration ratios for the cobalt-60 measurements. It is worth noting that for each calibration ratio, a background spectrum was taken, and subtracted from the cobalt-60 spectra. The computed ratios were then averaged to get an overall calibration factor, which was then used to determine the relevant fluences.

Table 3: Table of computed calibration factors.

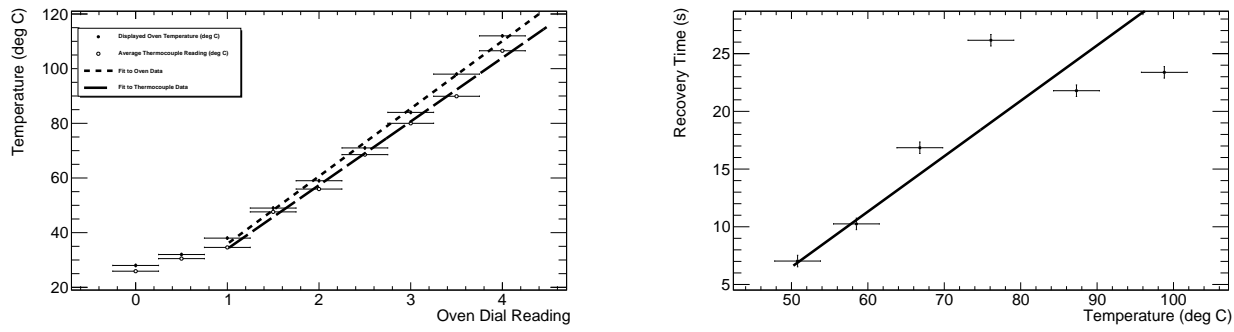
Position	1.17 MeV	1.33 MeV	1.17 Calibration Ratio	1.33 MeV Calibration Ratio
Counter	54553 ± 315	48289 ± 258	111.302 ± 1.366	118.617 ± 1.540
Calibrated	505 ± 28	419 ± 23		
Counter	54711 ± 315	48471 ± 259	107.901 ± 1.294	110.367 ± 1.544
Calibrated	512 ± 27	459 ± 32		
Counter	54309 ± 316	49216 ± 255	115.774 ± 1.617	112.363 ± 1.420
Calibrated	480 ± 33	439 ± 23		

$$\text{Average Calibration Factor} = 112.67 \pm 0.55$$

The error on the calibration factor was determined by the error due to the error on the counts, from MAESTRO, added in quadrature with half of the range of calibration factor values.

E Oven Calibration and Recovery Tests

Figure 27a shows how the temperature of the oven used for annealing, measured with both the thermocouple and the oven display, varies with the setting of the oven dial, which was an arbitrary scale from 1-10. It can be seen that above 40°C the relationship is linear. Since the temperature displayed by the thermocouple was more trustworthy than the displayed oven temperature, the thermocouple was used to set the oven temperature.



(a) Plot of the oven dial reading vs oven temperature.

(b) Plot of the oven temperature, measured with the thermocouple, vs the oven recovery time.

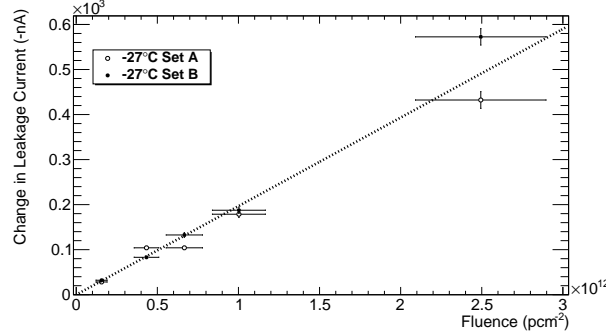
Figure 27: Oven calibration and recovery rate.

Figure 27b shows how the time required for the oven to recover, using a stopwatch, as a function of the oven temperature. The oven door was opened and closed over the course of about 5 seconds to simulate putting photodiodes into the oven. The time for the oven to get back to its original temperature was then measured. Due to the tenuous nature of figure 27b, a recovery time of 30 seconds was assigned to all annealing experiments. I.e. upon placing photodiodes in the oven, the initial oven temperature was taken 30 seconds after closing the door.

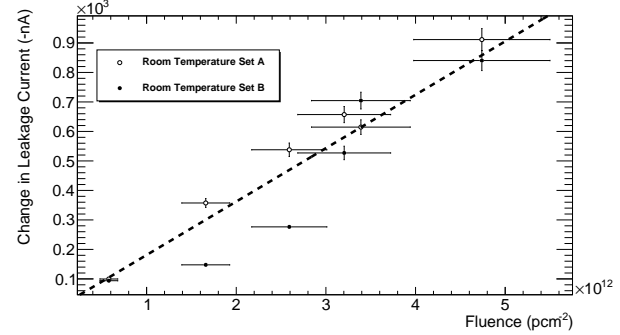
F Individual Data Sets for Hardness Factor Determination

Figure 28 shows the separate data sets for the two runs, used to determine the hardness factor of the MC40 cyclotron.

The gradients of the fits for figures 28a and 28b were $(1.97 \pm 0.11) \times 10^{-10}$ and $(1.81 \pm 0.09) \times 10^{-10}$ Acm² respectively. The corresponding current related damage rates were $\alpha_{-27^\circ\text{C}} = (9.33 \pm$



(a) Change in leakage current vs proton fluence for the -27°C data set.



(b) Change in leakage current vs proton fluence for the room temperature data set.

Figure 28: Individual data sets for ‘cold’ and ‘warm’ data sets.

$0.53) \times 10^{-17} \text{ Acm}^{-1}$ and $\alpha_{roomtemp} = (8.60 \pm 0.43) \times 10^{-17} \text{ Acm}^{-1}$, giving hardness factors of $\kappa_{MC40}^{-27^\circ\text{C}} = 2.34 \pm 0.13$ and $\kappa_{MC40}^{roomtemp} = 2.15 \pm 0.11$. Where ‘Set A’ and ‘Set B’ refer to the different sets in annealing. Figure 29 shows the same plot as shown in figure 24, but with the fits from the -27°C and room temperature data included.

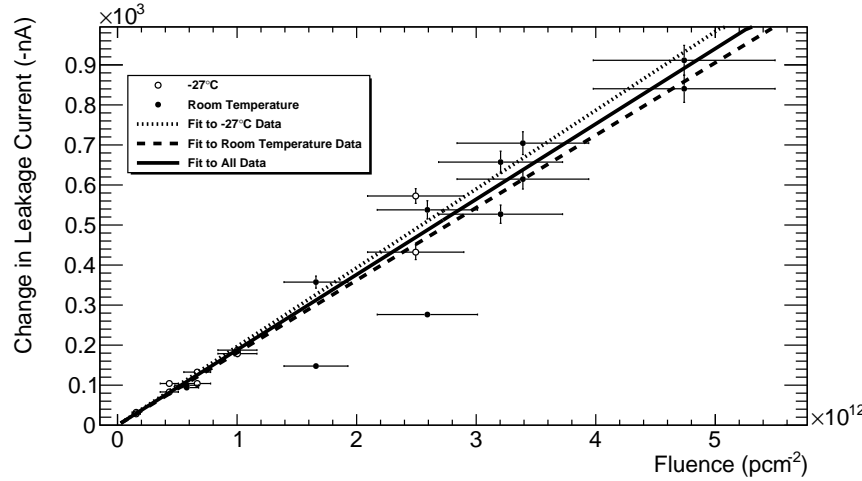


Figure 29: Change in leakage current vs proton fluence for all MC40 cyclotron data.

Table 4 displays the fluence applied to each photodiode, and the temperature of the irradiation. The fluences were scaled using a calibration factor of -27°C . Note, due to beam issues resulting in a higher fluence than expected, photodiodes 37 and 38 were omitted from the data.

Table 4: Table of fluences.

Preliminary		
Photodiode Number	Fluence (pcm^{-2})	Temperature of Irradiations ($^{\circ}\text{C}$)
7	$(1.15 \pm 0.18) \times 10^{12}$	-27
9	$(4.68 \pm 0.74) \times 10^{11}$	-27
10	$(5.24 \pm 0.83) \times 10^{12}$	-27
14	$(2.02 \pm 0.32) \times 10^{11}$	-27
6	$(1.15 \pm 0.18) \times 10^{12}$	-27
5	$(1.15 \pm 0.18) \times 10^{12}$	-27
3	$(5.24 \pm 0.83) \times 10^{12}$	-27
4	$(4.68 \pm 0.74) \times 10^{11}$	-27
8	$(1.15 \pm 0.18) \times 10^{12}$	-27
15	$(2.02 \pm 0.32) \times 10^{11}$	-27
Main		
Photodiode Number	Fluence (pcm^{-2})	Temperature of Irradiations ($^{\circ}\text{C}$)
26	$(5.79 \pm 1.0) \times 10^{11}$	Room Temperature
28	$(1.66 \pm 0.27) \times 10^{12}$	Room Temperature
30	$(2.59 \pm 0.42) \times 10^{12}$	Room Temperature
32	$(3.20 \pm 0.52) \times 10^{12}$	Room Temperature
34	$(4.74 \pm 0.76) \times 10^{12}$	Room Temperature
36	$(3.39 \pm 0.55) \times 10^{12}$	Room Temperature
25	$(5.79 \pm 1.0) \times 10^{11}$	Room Temperature
27	$(1.66 \pm 0.27) \times 10^{12}$	Room Temperature
29	$(2.59 \pm 0.42) \times 10^{12}$	Room Temperature
31	$(3.20 \pm 0.52) \times 10^{12}$	Room Temperature
33	$(4.74 \pm 0.76) \times 10^{12}$	Room Temperature
35	$(3.39 \pm 0.55) \times 10^{12}$	Room Temperature
38	$(1.40 \pm 0.22) \times 10^{13}$	-27
40	$(2.49 \pm 0.40) \times 10^{12}$	-27
42	$(6.67 \pm 0.11) \times 10^{11}$	-27
44	$(1.00 \pm 0.16) \times 10^{12}$	-27
46	$(4.33 \pm 0.76) \times 10^{11}$	-27
48	$(1.56 \pm 0.34) \times 10^{11}$	-27
37	$(1.40 \pm 0.22) \times 10^{13}$	-27
39	$(2.49 \pm 0.40) \times 10^{12}$	-27
41	$(6.67 \pm 0.11) \times 10^{11}$	-27
43	$(1.00 \pm 0.16) \times 10^{12}$	-27
45	$(4.33 \pm 0.76) \times 10^{11}$	-27
47	$(1.56 \pm 0.34) \times 10^{11}$	-27